Ultrasonics 96 (2019) 165–174

Contents lists available at ScienceDirect

Ultrasonics

journal homepage: www.elsevier.com/locate/ultras

Ultrasound Baseband Delay-Multiply-and-Sum (BB-DMAS) nonlinear beamforming

Che-Chou Shen*, Pei-Ying Hsieh

Department of Electrical Engineering, National Taiwan University of Science and Technology, Taipei, Taiwan

ARTICLE INFO

Keywords:
Adaptive imaging
Delay-Multiply-and-Sum (DMAS)
Baseband beamforming
Spatial coherence

ABSTRACT

Compared to conventional Delay-and-Sum (DAS) beamforming, Delay-Multiply-and-Sum (DMAS) imaging uses multiplicative coupling of channel pairs for spatial coherence of receiving aperture to improve image resolution and contrast. However, present DMAS imaging is based on the radio-frequency (RF) channel signals (RF-DMAS) and thus requires large oversampling to avoid aliasing and switching of band-pass filtering to isolate the corresponding spectral components for imaging. Baseband DMAS (BB-DMAS) beamforming in this study is based on the demodulated channel signals to provide similar results but with simplified signal processing. The BB-DMAS beamforming scales the magnitude of time-delayed channel signal by p-th root while maintaining the phase. After channel sum, the output dimensionality is restored by p-th power. The multiplicative coupling in BB-DMAS always renders baseband signal and thus the need for oversampling is eliminated. Besides, the BB-DMAS can use any rational p values to provide flexible image quality and an explicit relation between BB-DMAS beamforming and channel-domain phase coherence exists. Our results show that the image characteristics between BB-DMAS and RF-DMAS are similar. The suppression of lateral side lobe level, grating lobe level and uncorrelated random noises gradually increases with the rational p value in BB-DMAS beamforming. The image contrast improves from -24.8 dB in DAS to -34.3 dB, -43.0 dB and -51.4 dB in BB-DMAS, respectively with p value of 1.5, 2.0 and 2.5. In conclusion, BB-DMAS beamforming provides flexible manipulation of image quality by introducing baseband spatial coherence in the ultrasonic imaging.

1. Background

Ultrasound beamforming is performed by compensating the time delay of the received echo according to the geometric path of propagation for every channel in the array system. The delayed echoes in channels are coherently summed to amplify the signal from the on-axis direction and to suppress the interference from the off-axis direction. This process is commonly referred to as the delay-and-sum (DAS) beamforming. Though DAS beamforming is routinely utilized to produce the standard ultrasound image, it has several intrinsic drawbacks. First, the suppression of off-axis interference in the coherent sum depends mainly on the phase difference among channel waveforms and thus is generally insufficient for near-axis clutter. Second, for the echo coming from the direction of grating lobe, its coherent nature also produces noticeable image artifacts particularly when a longer pulse is utilized as excitation waveform. Consequently, DAS beamforming suffers from high lateral side-lobe level (LSLL) and noticeable grating lobe artifacts in the near field. These drawbacks lead to low image quality. Note that a smooth transmit-receive aperture apodization can help to suppress the LSLL but the lateral main-lobe width increases [1]. In other words, the design of aperture apodization results in a tradeoff between the image contrast and the image resolution. Moreover, the smooth apodization inevitably reduces the effective aperture size and thus degrades the signal-to-noise ratio.

In order to improve the image quality in DAS beamforming, many adaptive imaging methods have been proposed which can be grouped into two main categories. Methods in the first category achieve side-lobe suppression by directly constraining the side-lobe energy to optimize the apodization coefficient for each receive channel [2–6]. However, for every image pixel, the optimization process involves the inversion of the auto-covariance matrix of the received channel data and thus demands for huge computation especially when the number of channels is drastically high (e.g., in a 2-D array system). Similar difficulties also occur for methods involving the deconvolution of transmit beam pattern to estimate the interferences in the channel for compensation such as the parallel adaptive receive compensation algorithm

---

* Corresponding author at: Department of Electrical Engineering, National Taiwan University of Science and Technology, #43, Section 4, Keelung Road, Taipei 106 Taiwan.

E-mail address: choushen@mail.ntust.edu.tw (C.-C. Shen).

https://doi.org/10.1016/j.ultras.2019.01.010
Received 25 July 2018; Received in revised form 18 January 2019; Accepted 28 January 2019

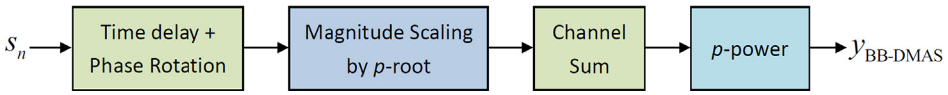

Fig. 1. Diagram of signal flowchart in the proposed BB-DMAS beamforming. When $p = 1$, the BB-DMAS degenerates to the conventional DAS beamforming.

Table 1
Simulation Parameters.

Transmit waveform	2-cycle Sinusoid
Center frequency	5 MHz
Bandwidth of Probe	90%
Number of elements	128
Number of scan lines	513
Line spacing	0.078 mm
Element pitch	0.31 mm
Element height	7 mm
Element width	0.308 mm
Kerf	2.5 um
Focal depth	30 mm
Sampling rate	100 MHz
Sound velocity	1540 m/s
Transmit F-number	1.5

Table 2
Experimental Parameters.

	Linear Array	Curved Array
Transmit waveform	2-cycle Sinusoid	2-cycle Sinusoid
Center frequency	5 MHz	4.4 MHz
Number of elements	128	128
Number of scan lines	153	209
Line spacing	0.23 mm	0.34°
Element pitch	0.31 mm	0.50 mm
Focal depth	30 mm	80 mm
Sampling rate	25.6 MHz	17.6 MHz
Sound velocity	1430 m/s	1540 m/s
Transmit F-number	2	2

[7–9]. On the contrary, methods in the second category avoid the appearance of image clutter by estimating the focusing quality for each image pixel and then the display magnitude of low-quality pixel is reduced. In other words, each pixel in the standard DAS image is multiplied by an adaptive weighting value based on its focusing quality. For example, the coherence factor (CF) can represent the focusing quality, which is defined as the ratio between the coherent power and the total power in the channel data [10]. By scaling the DAS image by the CF weighting, on-axis components are preserved due to its high coherent power while the off-axis components are relatively suppressed. It should be also noted that the CF weighting can also be represented in the form of Wiener postfilter [11]. Other definition of focusing factor also includes generalized coherence factor (GCF) [12], phase coherence factor (PCF) [13] and normalized cross-correlation between received echoes from complementary apertures [14].

Recently, a novel nonlinear beamforming has been proposed for ultrasound imaging by multiplying received radio-frequency (RF) echoes between every possible channel pair after time compensation. It is referred to as the delay-multiply-and-sum (DMAS) beamforming [15]. The purpose of channel-domain multiplication is to introduce the spatial coherence of channel data into the beamforming process. For clutters and noises, their spatial coherence rapidly drops as the spacing between channels increases. On the contrary, echoes from the main lobe generally exhibit higher coherence (i.e., high similarity) when being detected by channels in different spatial locations. Consequently, the side-lobe clutter and grating lobe artifacts can be suppressed in the beamforming output relative to the main-lobe signal. Note that the original form of RF-DMAS beamforming is computationally demanding due to the multiplication between every possible channel pairs. Therefore, a low computational cost formulation has been exploited and implemented in real-time on a research scanner [16]. Moreover, it can be generalized and further simplified by taking the square root of the absolute value of RF channel waveform before coherent summation [17]. Though the performance of RF-DMAS beamforming appears promising, its potential limitation is the sampling rate of the RF channel waveforms. Specifically, due to the multiplication of RF channel waveform, the original echoes at the f_0 imaging frequency will be spectrally shifted to the DC and the $2f_0$ frequency in the RF-DMAS beamforming. Since the RF-DMAS beamforming uses the $2f_0$ component for imaging, oversampling is required before channel multiplication to represent the $2f_0$ component without aliasing. Also, an additional band-pass filtering is required to extract the $2f_0$ component. Note that, when the original echoes contain the high-order harmonic component from the imaged object such as microbubble contrast agents [18], the required oversampling may further increase.

Inspired by the RF-DMAS beamforming, a baseband version of DMAS beamforming (BB-DMAS) is proposed in this study using the baseband spatial coherence instead of the original RF multiplication of channel waveform. In other words, the RF channel waveform is first demodulated and then the spatial coherence is estimated using the baseband channel data for imaging. Note that the proposed approach does not suffer from the aforementioned requirement of oversampling and the additional band-pass filtering because no spectral up-shifting is expected in the multiplication of baseband channel data. Consequently, the data rate in the proposed BB-DMAS beamforming remains the same as that in the conventional baseband DAS beamforming. Section 2 introduces the basics of BB-DMAS beamforming and its relation to the conventional DAS beamforming in terms of adaptive weighting. Section 3 describes the simulation methods and experimental setup in this study. Comparison of image quality between the proposed method and the adaptive weighting imaging method using both simulated and experimentally constructed B-mode image is presented in Section 4. Results are discussed in Section 5.

2. Theory

2.1. Baseband DAS (BB-DAS) beamforming

Baseband beamforming is a well-known alternative approach to achieve high focusing accuracy without oversampling. First, the channel waveforms are demodulated down to baseband and then the time delay is applied in a coarser temporal resolution. Finally, to correct the phase error produced in the demodulation process among different channels, phase rotation would be performed before coherent summation. Given the baseband channel data of the n-th channel after phase rotation $\mathrm{s}_n = a_n e^{j\phi_n} (a_n \geqslant 0)$ in the N-element array, the BB-DAS beamforming is performed by simply coherently summing the baseband channel data as shown in the following:

$$y_{\text{DAS}} = \frac{1}{N}\sum_{n=1}^{N} \mathrm{s}_n = \frac{1}{N}\sum_{n=1}^{N} a_n e^{j\phi_n} \tag{1}$$

2.2. BB-DMAS beamforming

Given the aforementioned channel data of the n-th channel, its magnitude-square-rooted version can be constructed as $\hat{\mathrm{s}}_n = \sqrt{a_n} e^{j\phi_n}$. In other words, the channel magnitude is scaled by taking its square root while the channel phase is kept unchanged. The proposed BB-DMAS beamforming is defined as the square of the coherent summation of the scaled channel data and can be formulated as

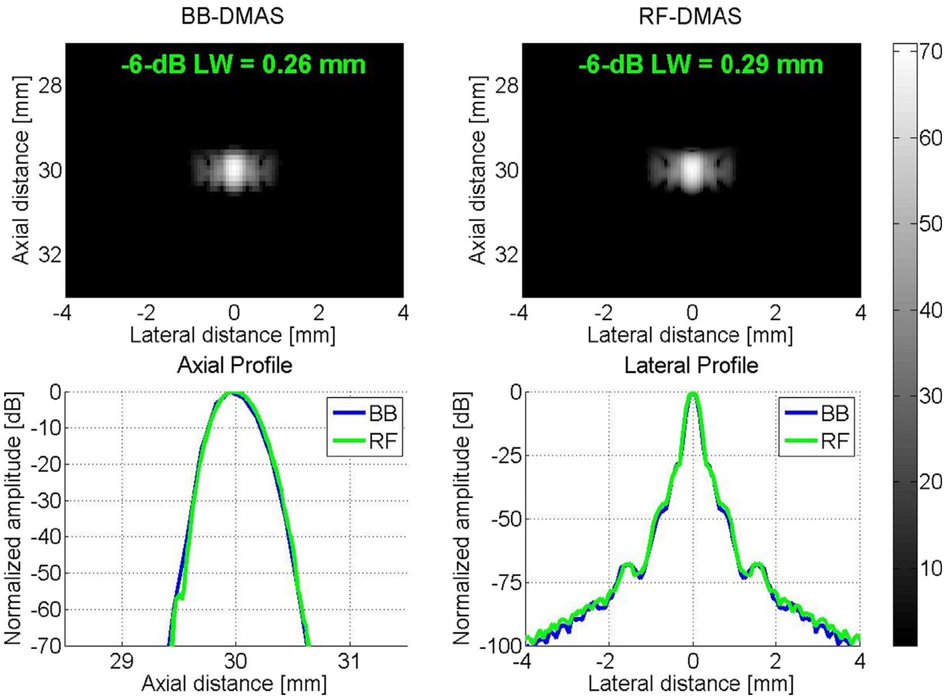

Fig. 2. Simulated PSFs and corresponding axial/lateral profiles in RF-DMAS and BB-DMAS (p = 2.0) beamforming. The −6-dB lateral width (LW) is provided for comparison of image lateral resolution.

$$y_{\text{BB-DMAS}} = \left(\frac{1}{N}\sum_{n=1}^{N}\hat{s}_n\right)^2 \tag{2}$$

Since the B-mode image is obtained by simply taking the absolute value of the beamforming output, the BB-DMAS beamforming will produce the B-mode image according to

$$\begin{aligned} |y_{\text{BB-DMAS}}| &= \left|\tfrac{1}{N}\textstyle\sum_{n=1}^{N}\hat{s}_n\right|^2 = \tfrac{1}{N^2}\left(\textstyle\sum_{n=1}^{N}\hat{s}_n\right)\left(\textstyle\sum_{n=1}^{N}\hat{s}_n\right)^* \\ &= \tfrac{1}{N^2}\left(\textstyle\sum_{n=1}^{N}\hat{s}_n\right)\left(\textstyle\sum_{n=1}^{N}\hat{s}_n^*\right) \\ &= \tfrac{1}{N^2}\textstyle\sum_{m=-N}^{N} R_{\hat{s}\hat{s}}(m) \end{aligned} \tag{3}$$

Note that the $R_{\hat{s}\hat{s}}(m)$ represents the autocorrelation of the magnitude-scaled channel data $\hat{\boldsymbol{S}} = [\hat{s}_1\ \hat{s}_2\ \hat{s}_3 \cdots\ \hat{s}_N]$across the entire active aperture at the m-th lag:

$$R_{xx}(m) = \begin{cases} \sum_{k=1}^{N-m} x_k x_{k+m}^* & m = 0,\ 1,\ 2. ..,(N-1) \\ \sum_{k=1}^{N+m} x_k^* x_{k-m} & m = -1,\ -2. ..,-(N-1) \end{cases} \tag{4}$$

In other words, the B-mode image in BB-DMAS beamforming is actually the integration of the entire autocorrelation function and thus corresponds to the spatial coherence of the magnitude-scaled channel data [19].

2.3. Relationship between BB-DMAS beamforming and BB-DAS beamforming

With the assumption that the magnitude variation among channels can be ignored (i.e., $a_n \cong a_0$ for $n = 1, 2, 3 \cdots N$), the relation between the BB-DMAS beamforming and the BB-DAS beamforming can be formulated as

$$\begin{gathered} \frac{y_{\text{BB-DMAS}}}{y_{\text{DAS}}} = \frac{\left(\frac{1}{N}\sum_{n=1}^{N}\hat{s}_n\right)^2}{\frac{1}{N}\sum_{n=1}^{N}s_n} = \frac{\left(\frac{1}{N}\sum_{n=1}^{N}\sqrt{a_0}e^{j\phi_n}\right)^2}{\frac{1}{N}\sum_{n=1}^{N}a_0e^{j\phi_n}} = \frac{\left(\frac{1}{N}\sum_{n=1}^{N}e^{j\phi_n}\right)^2}{\frac{1}{N}\sum_{n=1}^{N}e^{j\phi_n}} = \frac{1}{N}\sum_{n=1}^{N}e^{j\phi_n} \\ => \ |y_{\text{BB-DMAS}}| = \left|\frac{1}{N}\sum_{n=1}^{N}e^{j\phi_n}\right|\ |y_{\text{DAS}}| \end{gathered} \tag{5}$$

That is, the B-mode of BB-DMAS beamforming can be understood as the multiplication of the B-mode of DAS beamforming with a factor relating to the phase coherence among channels. Note that the assumption of $a_n \cong a_0$ holds particularly for high coherent target such as wire reflector. For low coherent target like speckle, it should be noted that the variation of channel magnitude may not be negligible. When the channel data across the aperture is highly coherent, the term $\left|{}^{1}\!/_{N}\sum_{n=1}^{N}e^{j\phi_n}\right|$ approaches unity, indicating the B-mode of BB-DMAS beamforming is similar to that of BB-DAS beamforming. On the contrary, $\left|{}^{1}\!/_{N}\sum_{n=1}^{N}e^{j\phi_n}\right|$ is smaller than unity if the channel data across the aperture is less coherent. Consequently, compared to the BB-DAS beamforming, the BB-DMAS beamforming would attenuate the low-coherence component in the received echoes such as the side-lobe clutter. Please note that the phase coherence factor is intrinsically included in the BB-DMAS beamforming. It does not demand for additional computation to estimate the weighting value of the conventional DAS output as proposed in [13].

2.4. Generalized p-th root BB-DMAS beamforming

The BB-DMAS beamforming can be generalized by maintaining the channel phase but adopting the p-th root of the channel magnitude. The approach is similar to that in [17] but the sign operation is not required. The diagram of signal flowchart is demonstrated in Fig. 1 and can be formulated as following:

$$y_{\text{BB-DMAS-}p} = \left(\frac{1}{N}\sum_{n=1}^{N}\sqrt[p]{a_n}\,e^{j\phi_n}\right)^p \tag{6}$$

Note that, in Fig. 1, the baseband channel data is firstly time-delayed with phase rotation to compensate the relative time-of-flight of channel waveforms. After the magnitude-scaled channel data is coherently summed, the p-th power is performed to recover the signal dimensionality.

Under the same assumption that $a_n = a_0$ for $n = 1, 2, 3 \cdots N$, the p-th root BB-DMAS beamforming can also be represented as the output of BB-DAS beamforming weighted by the (p-1)-th power of the

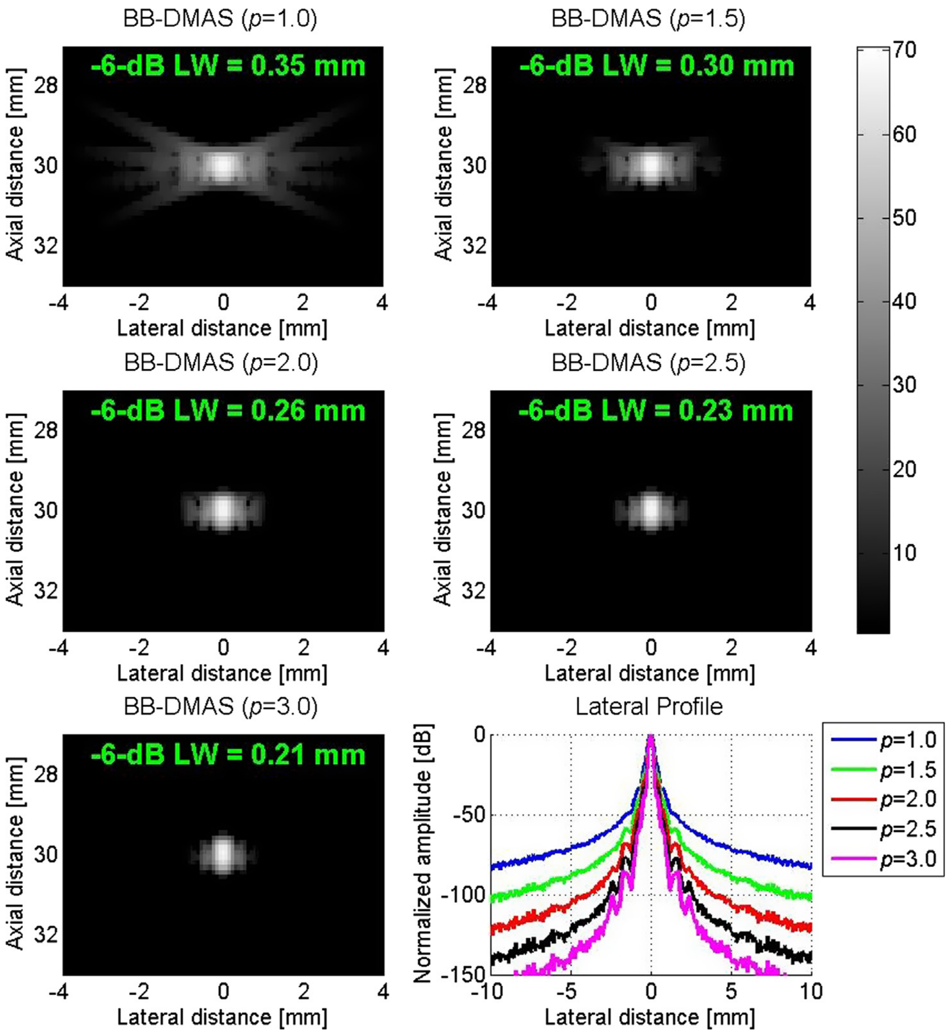

Fig. 3. Simulated PSFs in BB-DMAS beamforming with p value ranging from 1.0 to 3.0. The −6-dB lateral width (LW) is provided for comparison of image lateral resolution.

aforementioned phase coherence factor. When p is larger than two, the phase coherence weighting value is getting even smaller due to the operation of (p-1)-th power and thus the low-coherence component is further attenuated. In contrast, when p is smaller than two, the phase coherence weighting is approaching unity and the BB-DMAS beamforming performs more similar to the conventional BB-DAS beamforming.

$$\frac{y_{\text{BB-DMAS-}p}}{y_{\text{DAS}}} = \frac{\left(\frac{1}{N}\sum_{n=1}^{N}\sqrt[p]{a_n}\,e^{j\phi_n}\right)^p}{\frac{1}{N}\sum_{n=1}^{N}a_n e^{j\phi_n}} = \frac{\left(\frac{1}{N}\sum_{n=1}^{N}e^{j\phi_n}\right)^p}{\frac{1}{N}\sum_{n=1}^{N}e^{j\phi_n}} = \left(\frac{1}{N}\sum_{n=1}^{N}e^{j\phi_n}\right)^{p-1}$$
$$=> \ |y_{\text{BB-DMAS-}p}| = \left|\frac{1}{N}\sum_{n=1}^{N}e^{j\phi_n}\right|^{p-1} \ |y_{\text{DAS}}| \qquad (7)$$

2.5. Comparison between BB-DMAS beamforming and RF-DMAS beamforming

Though both the RF-DMAS beamforming and the proposed BB-DMAS beamforming rely on the spatial coherence in the channel domain to improve the image quality, several distinctions exist between them. First, the RF-DMAS beamforming is designed to perform on the RF channel waveform. The mutual multiplication among the RF channel waveforms upshifts the original spectrum from f_0 frequency to the $2f_0$ frequency and therefore a band-pass filtering operation is required to extract the $2f_0$ component for imaging. On the contrary, the proposed BB-DMAS beamforming is performed in the baseband channel data and thus is not limited by the requirement of additional band-pass filtering. Moreover, unlike the p-th root implementation of DMAS beamforming in [17] which demands for band-pass filtering at f_0 frequency when p is odd integer or band-pass filtering at $2f_0$ frequency when p is even integer, the BB-DMAS beamforming does not change with the selection of p value because the channel data has been demodulated into the baseband before beamforming. Specifically, the generalized p-th root BB-DMAS beamforming uses the same signal processing for any selection of p value and the p value is no longer limited to integer value. This simplifies the implementation of BB-DMAS beamforming and also makes the manipulation of image quality much more flexible. Second, the RF-DMAS beamforming also potentially produces a new pair of grating lobes which is closer to the mainlobe direction due to the doubled center frequency in the RF channel multiplication [15]. In contrast, the proposed BB-DMAS beamforming is immune to this artifact because of its baseband nature.

3. Research method

3.1. Simulation setup

Two types of imaged objects – point reflectors and speckle-generating phantom are simulated respectively for evaluation of point-spread-function (PSF) and image contrast in the presence of cyst region. The simulation is based on the Field II program [20–21] with the

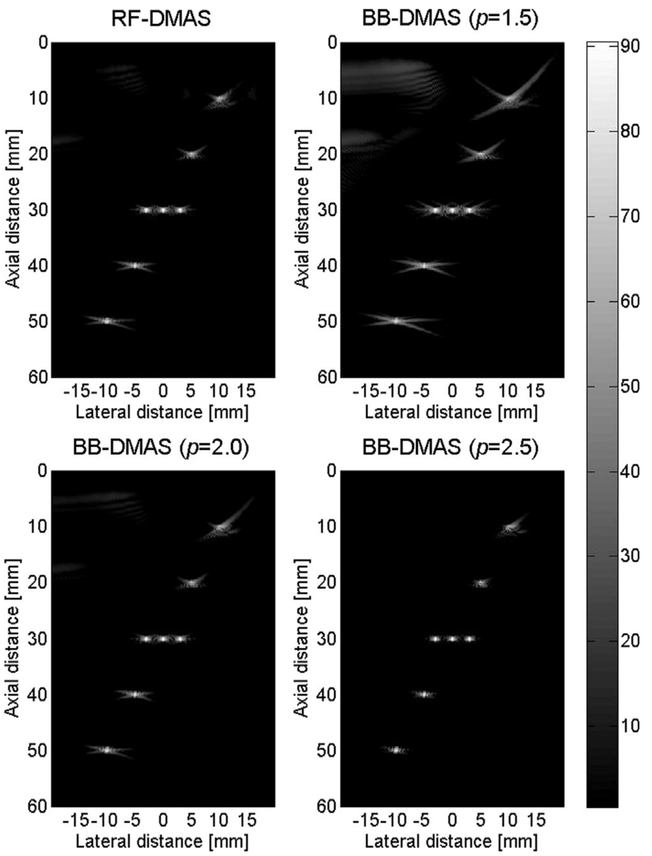

Fig. 4. Simulated B-mode images of wire matrix in RF-DMAS and BB-DMAS beamforming with p value ranging from 1.5 to 2.5.

parameters listed in Table 1. For PSF, a single point target is placed at the transmit focal depth of 30 mm. In addition, matrix of point reflectors was also considered. In a speckle-generating phantom, hypoechoic cyst, anechoic cyst and hyperechoic cyst having radius of 3 mm are placed at the transmit focal depth. The phantom has a size of 30 mm × 10 mm × 1 mm, respectively in the lateral, axial, and elevational directions and a density of about 10 scatterers per resolution cell. For the hypoechoic cyst, various scattering magnitudes of −18 dB, −12 dB and −6 dB relative to the image background are considered in separate simulations when the corresponding scattering magnitude of the hyperechoic cyst is respectively set to be +18 dB, +12 dB and +6 dB. Therefore, there are a total of 7 different scattering magnitude (i.e., −18 dB, −12 dB, −6 dB, +6 dB, +12 dB, +18 dB and anechoic) in the speckle-generating simulations. Moreover, point reflectors with scattering magnitude of 26 dB higher than the background are also included in the speckle simulation as a reference.

The proposed BB-DMAS beamforming with different p values are compared with RF-DMAS beamforming. For RF-DMAS, its implementation is based on the equivalent formulation proposed in [16] and the dominant signal component at about twice the transmit frequency is extracted after beamforming using a 64-tap FIR filter at a sampling rate of 100 MHz. For BB-DMAS, the simulated channel data at a reduced sampling rate of 25 MHz is firstly demodulated to baseband and then time-delayed with phase rotation to compensate the relative time-of-flight of channel waveforms. The BB-DMAS beamforming scales the magnitude of time-delayed channel signal by p-th root while maintaining the phase. After channel summation of the magnitude-scaled channel data, the output dimensionality is restored by p-th power to provide the BB-DMAS beamforming as indicated in the Section 2.4. Moreover, the CF weighting method is also performed as a benchmark of adaptive imaging for comparison of image contrast. For CF-weighted image, the time-delayed baseband channel data without

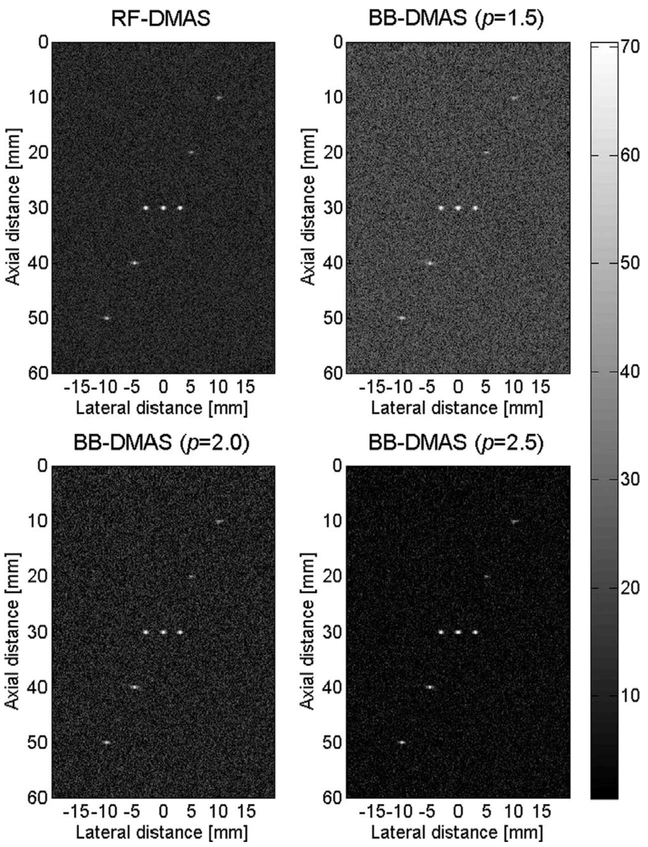

Fig. 5. Simulated B-mode images of wire matrix in RF-DMAS and BB-DMAS beamforming with p value ranging from 1.5 to 2.5. White Gaussian noise is included with a channel SNR of 10 dB.

magnitude scaling (i.e, $p = 1$) are coherently summed and then multiplied with a weighting value which represents the ratio of DC component relative to the total components in the power spectrum of channel data. Specifically, the CF weighting value is calculate using the following equation [10]:

$$\mathrm{CF} = \frac{\left|\sum_{i=1}^{N} s_n\right|^2}{N\sum_{i=1}^{N} |s_n|^2} \tag{10}$$

Note that, for all beamforming methods in this study, the receive aperture size is the active area of the entire probe and thus no dynamic apodization is used.

3.2. Experimental setup

Experimental measurements are performed using Prodigy ultrasound imaging system (S-sharp Corporation, New Taipei City, Taiwan) with a 128-element linear array probe to acquire the pre-beamforming channel waveforms. The linear array has a pitch of 0.31 mm and a center frequency of 5 MHz. A commercial ultrasound phantom (model 549, ATS Laboratories, Bridgeport, CT. USA) was used as the imaged object. Images of the ATS phantom are acquired by setting the transmission focal depth at 30 mm using two different scanning view. One includes the anechoic cysts for evaluation of image contrast and the other contains the wire reflectors for evaluation of image resolution. In addition to the phantom measurements, *in vivo* channel waveforms are also acquired from the kidney of a 38-year-old male volunteer with a 4.4-MHz curved linear array by setting the transmission focal depth at 80 mm. Note that the channel waveforms are recorded at a sampling rate of four times of the center frequency of the transducer in both phantom and *in vivo* measurements. The experimental imaging

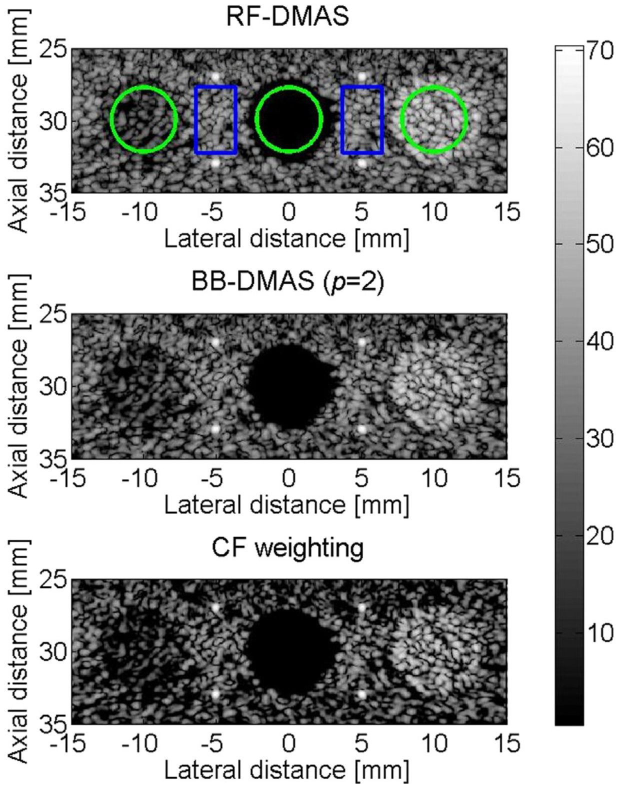

Fig. 6. Simulated B-mode images of speckle-generating phantom with ± 12-dB cyst inclusions in RF-DMAS and BB-DMAS ($p = 2$) beamforming. Adaptive CF weighting is also provided for comparison.

parameters are listed in Table 2.

3.3. Image quality metrics

The image contrast is quantitatively calculated by two parameters: the contrast ratio (CR) and the contrast-to-noise ratio (CNR). The CR value is defined as the ratio of the mean value in the cyst region to that in the background region. It can be formulated as $\mathrm{CR} = 20\log_{10}(\mu_{cyst}/\mu_{bck})$ where μ_{cyst} and μ_{bck} are the mean image values before log-compression inside the cyst and in the background region, respectively. The CNR value takes the speckle variation into consideration by dividing the absolute value of image contrast by the standard deviation before log-compression. Its formulation is $\mathrm{CNR} = |\mu_{cyst} - \mu_{bck}|/\sqrt{\sigma_{cyst}^2 + \sigma_{bck}^2}$ where σ_{cyst} and σ_{bck} represents the standard deviation, respectively in the cyst and the background. In order to quantify the image resolution, the −6-dB lateral width of wire reflector at the focal depth is also compared among different beamforming methods.

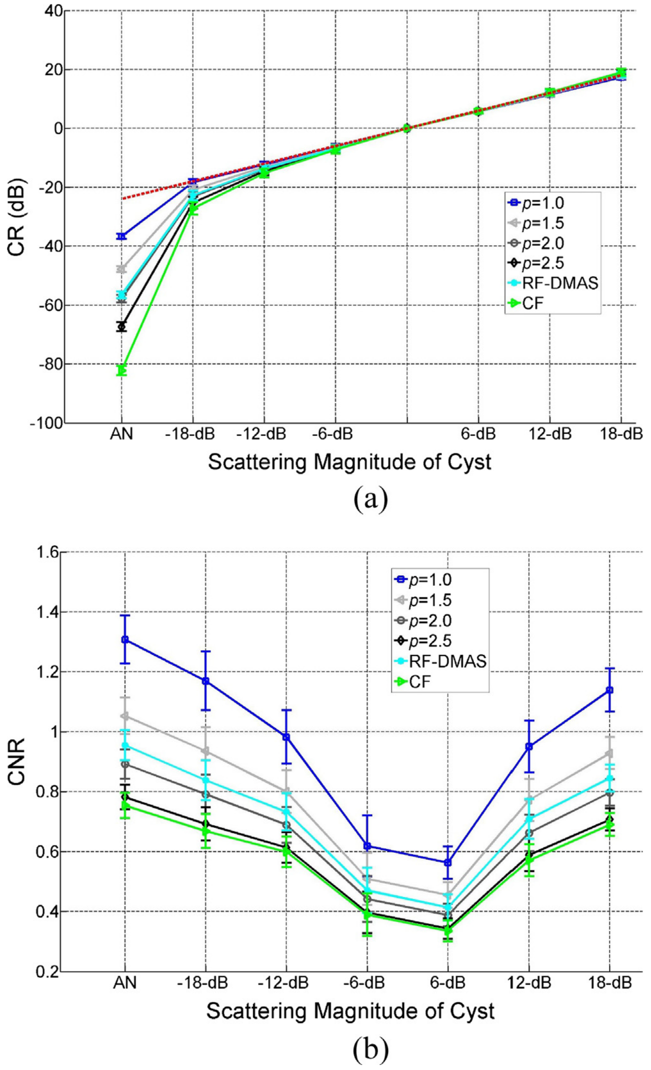

Fig. 7. Quantitative analyses of image contrast as a function of scattering magnitude in the cyst region. (a) contrast ratio (CR) and (b) contrast-to-noise ratio (CNR).

4. Results

4.1. Simulations

In Fig. 2, the PSFs at the focal depth of BB-DMAS and RF-DMAS beamforming are demonstrated in the upper panels with a display dynamic range of 70 dB while their lateral and axial profiles are provided in the lower panels. For the BB-DMAS, the p value is set to be two in order to provide a fair comparison with the RF-DMAS. As can be seen in the upper panels of Fig. 2, the PSF image of BB-DMAS resembles that of RF-DMAS when the p value is equal to 2. The axial profiles of BB-DMAS and RF-DMAS appear to be similar to each other, indicating that they have the same image axial resolution. Also, both RF-DMAS and BB-DMAS beamforming exhibit similar level of lateral side lobe and thus should provide similar image contrast. For comparison of image lateral resolution, the corresponding −6-dB lateral width (LW) in Fig. 2 is 0.26 mm and 0.29 mm, respectively for BB-DMAS and RF-DMAS. The PSFs of BB-DMAS beamforming with p value ranging from 1.0 to 3.0 are also represented in Fig. 3. Note that BB-DMAS beamforming with $p = 1.0$ is actually the same as conventional DAS. The corresponding lateral beam patterns at the depth of 30 mm are also illustrated. Fig. 3 shows BB-DMAS is capable of providing flexible and continuously tunable manipulation of the lateral side lobe level by changing the p value to any rational value. Moreover, the image lateral resolution of BB-DMAS beamforming also improves with the p value.

Simulations of wire matrix were also performed to study the achievable grating lobe rejection in BB-DMAS beamforming as shown in Fig. 4. Note that, due to the wideband transmit waveform in ultrasound imaging, echoes from grating lobe direction also has lower coherence in the channel-domain as compared to those from main lobe direction. In Fig. 4, the display dynamic range is increased to 90 dB in order to observe the grating lobe artifacts in the B-mode images of the wire matrix. Though the BB-DMAS beamforming with $p = 1.5$ still exhibits noticeable grating lobe artifacts especially for wires at the depth of 10 mm and 20 mm, the achievable suppression of grating lobe level increases with the p value. Actually, for p value greater than 2, the aforementioned grating lobes becomes almost invisible. Note that the RF-DMAS

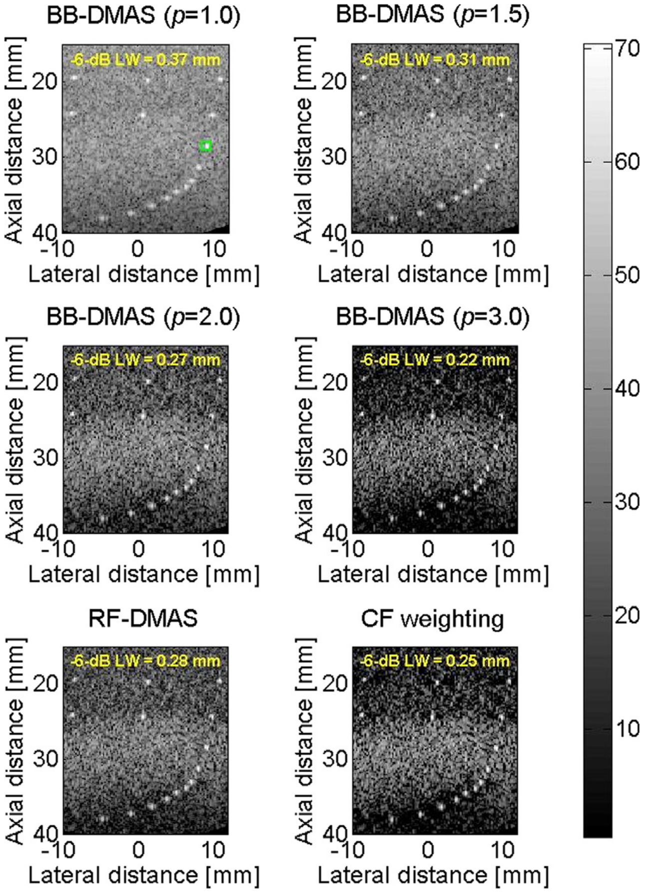

Fig. 8. Experimental B-mode images of wire matrix in speckle-generating phantom using BB-DMAS beamforming with p value ranging from 1.0 to 3.0 and CF weighting. The RF-DMAS counterpart is also included for comparison. The green rectangle indicates the wire at transmit focal depth for evaluation of −6-dB lateral width (LW). (For interpretation of the references to colour in this figure legend, the reader is referred to the web version of this article.)

beamforming also provides comparable suppression of grating lobe level to the BB-DMAS counterpart with $p = 2.0$. B-mode image of the same wire matrix was also simulated by including white Gaussian noise into the channel waveforms of each scan line. The channel SNR is set to be 10 dB. Fig. 5 shows that BB-DMAS beamforming provides effective noise rejection, showing that the noise level in the image background markedly decreases with the p value. This observation indicates that measurement of channel coherence in BB-DMAS beamforming helps to suppress the noisy background while keeping the coherent source such as the point reflectors visually detectable. Again, it is also noticeable that the BB-DMAS beamforming with $p = 2.0$ provides comparable suppression of uncorrelated random noises to the RF-DMAS counterpart.

Simulated B-mode images of speckle-generating phantom with cyst inclusions are demonstrated in Fig. 6 using RF-DMAS and BB-DMAS ($p = 2$) beamforming, respectively in the upper and the middle panels. Adaptive CF weighting is also performed for comparison. In Fig. 6, the left cyst has a −12-dB scattering magnitude relative to the image background while the right cyst has a +12-dB scattering magnitude. The middle cyst is anechoic and is surrounded by four wires. Similar to the RF-DMAS beamforming and the adaptive CF weighting, the image clutter within the anechoic cyst has been effectively removed by the proposed BB-DMAS beamforming. Nonetheless, it should be noted that the CF weighted image exhibits more granular appearance in the background speckle pattern. Quantitative analyses of CR and CNR of the cyst region with various scattering magnitude ranging from −18 dB to +18 dB are shown in Fig. 7 for comparison of RF-DMAS, BB-DMAS with different p value and CF-weighting. The CR and CNR values are estimated using the [1]blue rectangles and the green circles in Fig. 6, respectively as the background region and the cyst region. Note that a straight red line is included in the panel (a) to represent the reference CR value which is determined by the scattering magnitude of the cyst relative to that of the background in the simulation setup. Both DMAS beamforming and CF weighting tend to over-estimate the CR value for hypoechoic cyst while they agree well with the reference line for hyperechoic cyst. The performance of BB-DMAS gradually converges to the performance of CF-weighting when the p value increases. For example, for the −12-dB hypoechoic cyst, the estimated CR is −14.5 dB, −13.8 dB and −13.1 dB, respectively for BB-DMAS with $p = 2.5$, $p = 2.0$ and $p = 1.5$. In contrast, the CR is −15.2 dB and −13.7 dB for the CF weighting and RF-DMAS, respectively. Note that the BB-DMAS beamforming with $p = 2.0$ has a CR value similar to the RF-DMAS counterpart. Fig. 7(a) also shows that, for the anechoic cyst, the CR in BB-DMAS beamforming markedly improves with the p value but remains inferior to that in CF-weighting. For example, the estimated CR for the anechoic cyst drastically boost from −58 dB in the BB-DMAS beamforming with $p = 2.0$ to −82 dB in CF weighting.

In Fig. 7(b), however, results indicate that the BB-DMAS beamforming with $p = 1.0$ (i.e., conventional DAS) still provides the highest CNR for all types of cyst compared to BB-DMAS, RF-DMAS and CF weighting. This is due to the smooth speckle pattern in DAS beamforming. In contrast, though the CF weighting generally achieves the highest image contrast for hypoechoic cyst (e.g., the lowest estimated CR value in Fig. 7(a)), its CNR is considerably lower than both BB-DMAS and RF-DMAS beamforming since the coherence weighing tends to produce more granular speckle pattern and thus noticeably elevate the background speckle variation. Moreover, the RF-DMAS appears to have a higher CNR than the BB-DMAS with $p = 2.0$ even though they have virtually the same PSF as shown in Fig. 2. However, it should be noted that BB-DMAS beamforming with $p = 1.5$ has the highest CNR performance relative to the BB-DMAS with higher p values and the RF-DMAS. Consequently, BB-DMAS appears to provide a flexibly tunable tradeoff by manipulating the p value to increase the CR without excessive loss of CNR.

4.2. Experiments

Experimental B-mode images of speckle-generating ATS phantom using BB-DMAS beamforming with p value ranging from 1.0 to 3.0 are demonstrated in Fig. 8 and Fig. 9, respectively for wire reflectors and anechoic cysts. The CF weighting method is also provided for comparison. Note that, when the imaged object has a much higher echogenicity than the speckle background such as the wires reflectors, CF-weighted image tends to exhibit marked black-region artifacts around the wire reflectors. This is particular obvious especially in the region away from the transmit focal depth. For example, the presence of wire reflectors at the depth of 24 mm would be regarded as the incoherent interference to nearby speckle background and thus an abrupt decrease of the coherence factor occurs. Consequently, the wire reflector in CF-weighted image appears to be a white spot with a pair of black wing in the lateral direction. In contrast, this kind of over-attenuation of speckle background in the vicinity of strong reflectors is relatively alleviated in BB-DMAS beamforming especially when $p = 1.5$ and 2.0. Moreover, the image resolution in BB-DMAS beamforming also improves with the p value. For the wire reflector at the focal depth (i.e., 30 mm) as indicated by the green box, its −6-dB LW decreases from 0.37 mm with $p = 1.0$ to 0.31 mm, 0.27 mm and 0.22 mm, respectively with p value of 1.5, 2.0 and 3.0. Though the CF-weighted image also has comparable lateral

---

[1] For interpretation of color in Fig. 6, the reader is referred to the web version of this article.

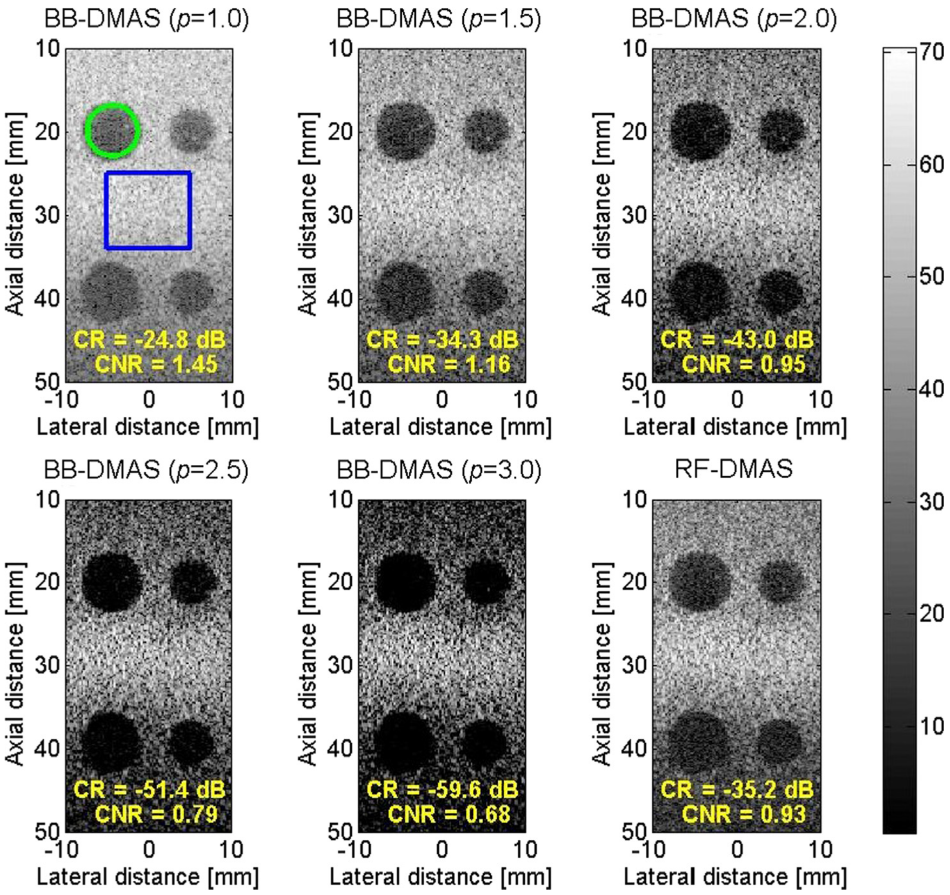

Fig. 9. Experimental B-mode images of anechoic cysts in speckle-generating phantom using BB-DMAS beamforming with p value ranging from 1.0 to 3.0. The green circle and blue rectangle indicate the region of interest for evaluation of image contrast. The RF-DMAS counterpart is also included for comparison. (For interpretation of the references to colour in this figure legend, the reader is referred to the web version of this article.)

width of 0.25 mm, it will not be included in the subsequent B-mode images due to the presence of severe black-wing artifacts in the image background. For comparison, the RF-DMAS counterpart is also provided and it appears visually similar to the BB-DMAS with $p = 2.0$.

Fig. 9 shows that BB-DMAS beamforming provides improved CR when the selection of p value increases. Nonetheless, the CNR of BB-DMAS image decreases with p value due to the increased speckle variation in nonlinear beamforming. Note that, among all p values higher than unity, the CNR with $p = 1.5$ is the highest which is consistent with the simulations. Though the RF-DMAS image also provides CR improvement, the achievable CR remains inferior to that of BB-DMAS with $p = 2.0$. This is probably due to the distortion of PSF when the RF-DMAS is implemented at a lower sampling rate. Fig. 10 shows the *in vivo* B-mode images of kidney using BB-DMAS beamforming with p value of 1.0 and 1.5., respectively in panel (a) and (b) for comparison. It should be noted that BB-DMAS beamforming with $p = 1.0$ is actually the same as the conventional DAS. The RF-DMAS counterpart is also provided in panel (c) for comparison. In BB-DMAS beamforming, the p value is selected to be 1.5 due to its highest CNR as indicated in Fig. 9. The quality of Fig. 10(b) is clearly improved as compared to that of Fig. 10(a) due to higher image contrast. Note that the clutter artifacts and reverberations which appear as foggy mask in Fig. 10(a) generally have low spatial coherence in the channel domain. Therefore, after removing these image artifacts using BB-DMAS beamforming with p value higher than unity, the anatomical structures of kidney such as the renal pelvis can be better highlighted.

5. Discussions and conclusions

In this study, the delay-multiply-and-sum (DMAS) beamforming has been extended to baseband (BB) implementation by p-th root scaling the magnitude of baseband channel signal but preserving its phase information. After coherent summation of the magnitude-scaled channel signal and restoring the signal dimensionality by p-th power, the resultant BB-DMAS beamforming is capable of suppressing lateral side lobe level and grating artifacts together with random noises in the B-mode image. Compared to its radio-frequency (RF) counterpart, the proposed BB-DMAS beamforming has several advantages. First, the data rate in BB-DMAS beamforming remains the same as that in the conventional baseband DAS beamforming Specifically, in order to avoid spectral aliasing, oversampling is required in RF-DMAS beamforming to accommodate the artificial $2f_0$ spectral component.

Using the formulation in [16], it can be derived that RF-DMAS requires one sign, two absolute value, one square root and two additions for each data sample per channel. For BB-DMAS, however, both the real and the imaginary part of each complex sample per channel require one square root and one addition. Assuming that the data rate of RF-DMAS is twice higher than that of BB-DMAS due to oversampling, BB-DMAS can eliminate a total of two sign, four absolute value and two additions relative to RF-DMAS for the same temporal segment per channel. Note that a complete analysis of computational complexity should also consider the intrinsic distinction between BB beamforming and RF beamforming such as the number of demodulator and the effect of data rate on time compensation. This is however beyond the scope of this study and will be addressed in the future work.

In the case of harmonic RF-DMAS beamforming as in [22], the required oversampling is even more severe. For example, the second harmonic signal at $2f_0$ frequency in the output of RF-DMAS beamforming will be spectrally shifted to $4f_0$ frequency. Consequently, a very high sampling rate (up to $16f_0$) is required by either an expensive analog-to-digital converter or extensive interpolation. This dramatically increases the sample number for every image line. On the contrary, the proposed BB-DMAS beamforming is performed using the BB channel data and thus is not limited by the requirement of oversampling. The

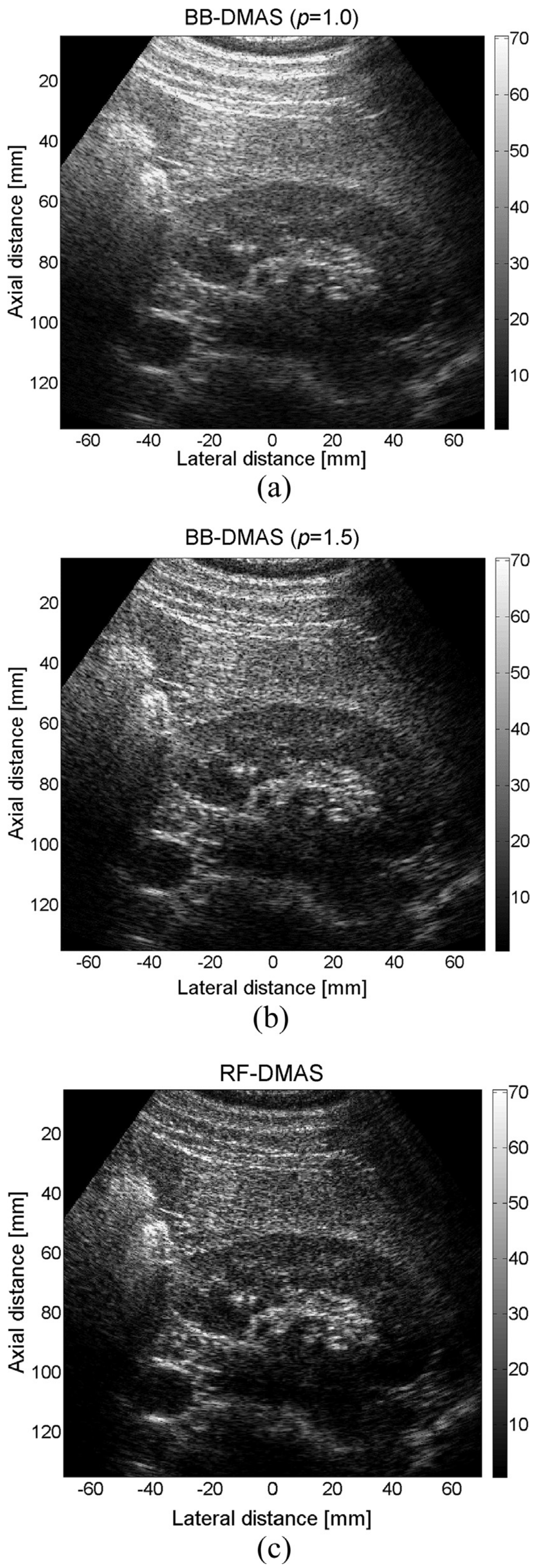

Fig. 10. *in-vivo* B-mode images of human kidney using BB-DMAS beamforming with p value of 1.0 and 1.5. The RF-DMAS counterpart is also included for comparison.

baseband nature also makes the manipulation of image quality highly tunable in the proposed BB-DMAS beamforming. In other words, unlike the RF implementation in [17] which only considers the integer p value, the performance of BB-DMAS beamforming can be fine-tuned by adopting any rational p value. Note that an improved version of the work in [17] has recently been developed as the p-DAS beamforming [23]. Similar to BB-DMAS, p-DAS beamforming is also capable of continuous tuning the image quality by any rational p value, it is believed that the two works are equivalent to each other except that one is for RF beamforming and the other is for BB beamforming. Both methods rely on the p-th root and p-th power to scale the echo magnitude before and after channel sum. However, the preservation of channel phase is performed by the sign operation in p-DAS beamforming while the BB-DMAS keeps the baseband phase unchanged instead.

Moreover, BB-DMAS beamforming always uses the same processing flow regardless the selection of p value. It does not suffer from the switching of imaging band as the p value changes from even integer to odd integer in the RF implementation. Though the BB-DMAS image appears visually similar to the RF-DMAS counterpart, the BB-DMAS actually shows higher image contrast in the case of anechoic cysts due to the undistorted PSF with a low sampling rate.

Note that a connection between the output of BB-DMAS beamforming and the integration of channel-domain autocorrelation function has been established in this study. Consequently, the BB-DMAS image actually represents similar spatial coherence of the received echoes in Short Lag Spatial Coherence (SLSC) imaging [19] but without normalization. Therefore, the difference in echo intensity is still preserved in the BB-DMAS image as in the conventional DAS image. Nonetheless, the combination of both spatial coherence and the echo intensity in BB-DMAS beamforming inevitably leads to noticeable highlighting effect of the focal zone. That is, since the backscattering signal from the focal zone has both higher spatial coherence and echo intensity, the resultant BB-DMAS image brightness of the focal zone is generally markedly higher than that out of the focal zone even in a homogeneous speckle-generating object. This phenomenon appears to be particularly obvious in B-mode imaging with small F-number (i.e., strong focusing) as shown in Figs. 8 and 9. Moreover, when a larger p value is utilized in BB-DMAS beamforming, the image brightness out of the focal zone would become more attenuated and only the transmit focal zone remains detectable in BB-DMAS beamforming. This is because, in the case of high p value, the image brightness is dominated mostly by the spatial coherence and thus the highlighting effect of the focal zone gets intensified. In order to compensate the highlighting effect of the focal zone, BB-DMAS beamforming can be integrated with total focusing technique such as the synthetic transmit aperture [24–26] and coherent plane wave compounding [27] as suggested for the SLSC imaging [28]. Similar approaches have been verified for RF-DMAS beamforming [29–30] and thus are expected to work well for the proposed BB-DMAS beamforming.

Compared to the adaptive weighting method, our results also show that the BB-DMAS beamforming suffer less from the black wing artifact of the image background in the lateral vicinity of strong echoic target in the case of $p = 1.5$ and 2. This is also because the BB-DMAS beamforming provides not only spatial coherence but also echo intensity. Specifically, even though the overall spatial coherence is significantly reduced when the nearby strong echoic target acts as dominant side lobe, the echo intensity of the background speckle is still preserved in the output of BB-DMAS beamforming. On the contrary, no matter whether the signal coherence is represented by the coherence factor in [10,12] or phase coherence factor in [13], this coherence value is utilized to weight the final B-mode image intensity and thus would mask out any low-coherence structure in adaptive-weighted images. Nonetheless, it should be also noted that the performance of BB-DMAS beamforming would approach that of adaptive weighting method when a higher p value is utilized. This artifact is inherent to all coherence-based beamforming including DMAS [31]. Similarly, the CR in the hypoechoic cyst as shown in Fig. 7(a) gets under-estimated due to the loss of signal coherence when the echo magnitude from the main lobe is lower than that from the side lobe. Specifically, since echoes from the side lobe exhibit lower spatial coherence in the received channel, the total signal coherence degrades when the contribution from side lobe dominates. By utilizing a higher *p* value to emphasize the spatial coherence, the phenomenon becomes more obvious in BB-DMAS beamforming and appears similar to that in CF weighting.

Since the proposed BB-DMAS beamforming maintains the same phase of channel data as DAS beamforming, its application may be further extended from B-mode imaging to other imaging modes in which the phase information is crucial. The capability of BB-DMAS beamforming in suppressing incoherent interferences is expected to improve the motion detection such as in Doppler mode and shear wave elastography and thus will be the focus of our future work.

Acknowledgments

This work was supported by the Ministry of Science and Technology of Taiwan under Grant No. 106-2221-E-011-026-MY2.

Appendix A. Supplementary material

Supplementary data to this article can be found online at https://doi.org/10.1016/j.ultras.2019.01.010.

References

[1] G. Cardone, C. Cincotti, P. Gori, M. Pappalardo, Optimization of wide band linear arrays, IEEE Trans. Ultrason. Ferroelectr. Freq. Control 48 (2001) 943–952.

[2] J.-F. Synnevag, A. Austeng, S. Holm, Adaptive beamforming applied to medical ultrasound imaging, IEEE Trans. Ultrason. Ferroelectr. Freq. Control 54 (2007) 1606–1613.

[3] J.F. Synnevag, A. Austeng, S. Holm, Benefits of minimum variance beamforming in medical ultrasound imaging, IEEE Trans. Ultrason. Ferroelectr. Freq. Control 56 (2009) 1868–1879.

[4] C.-I.C. Nilsen, I. Hafizovic, Beamspace adaptive beamforming for ultrasound imaging, IEEE Trans. Ultrason. Ferroelectr. Freq. Control 56 (2009) 2187–2197.

[5] S.-L. Wang, P.-C. Li, MVDR-based coherence weighting for high-frame-rate adaptive imaging, IEEE Trans. Ultrason. Ferroelectr. Freq. Control 56 (2009) 2097–2110.

[6] A.E.A. Blomberg, I.K. Holfort, A. Austeng, J.F. Synnevag, S. Holm, J.A. Jensen, APES beamforming applied to medical ultrasound imaging, Proc. IEEE Ultrason. Symp. (2009) 2347–2350.

[7] P.C. Li, S.W. Flax, E.S. Ebbini, M. O'Donnell, Blocked element compensation in phased array imaging, IEEE Trans. Ultrason. Ferroelectr. Freq. Control 40 (1993) 283–292.

[8] S. Krishnan, P.-C. Li, M. O'Donnell, Adaptive compensation of phase and magnitude aberrations, IEEE Trans. Ultrason. Ferroelectr. Freq. Control 43 (1996) 44–55.

[9] S. Krishnan, K.W. Rigby, M. O'Donnell, Efficient parallel adaptive aberration correction, IEEE Trans. Ultrason. Ferroelectr. Freq. Control 45 (1998) 691–703.

[10] K.W. Hollman, K.W. Rigby, M. O'Donnell, Coherence factor of speckle from a multi-row probe, Proc. IEEE Ultrason. Symp. (1999) 1257–1260.

[11] C.-I.C. Nilsen, S. Holm, Wiener beamforming and the coherence factor in ultrasound imaging, IEEE Trans. Ultrason. Ferroelectr. Freq. Control 57 (2010) 1329–1346.

[12] P.-C. Li, M.-L. Li, Adaptive imaging using the generalized coherence factor, IEEE Trans. Ultrason. Ferroelectr. Freq. Control 50 (2003) 128–141.

[13] J. Camacho, M. Parrilla, C. Fritsch, Phase coherence imaging, IEEE Trans. Ultrason. Ferroelectr. Freq. Control 56 (2009) 958–974.

[14] C. Seo, J.T. Yen, Sidelobe suppression in ultrasound imaging using dual apodization with cross-correlation, IEEE Trans. Ultrason. Ferroelectr. Freq. Control 55 (2008) 2198–2210.

[15] G. Matrone, A.S. Savoia, G. Caliano, G. Magenes, The delay multiply and sum beamforming algorithm in ultrasound B-mode medical imaging, IEEE Trans. Med. Imag. 34 (2015) 940–949.

[16] A. Ramalli, M. Scaringella, G. Matrone, A. Dallai, E. Boni, A.S. Savoia, L. Bassi, G.E. Hine, P. Tortoli, High dynamic range ultrasound imaging with real-time filtered-delay multiply and sum beamforming, Proc. IEEE Ultrason Symp, 2017.

[17] M. Polichetti, F. Varray, G. Matrone, A.S. Savoia, J.C. Béra, C. Cachard, B. Nicolas, A computationally efficient nonlinear beamformer based on p-th root signal compression for enhanced ultrasound B-mode imaging, Proc. IEEE Ultrason Symp, 2017.

[18] W.T. Shi, F. Forsberg, Ultrasonic characterization of the nonlinear properties of contrast microbubbles, Ultrasound Med. Biol. 26 (2000) 93–104.

[19] M.A. Lediju, G.E. Trahey, B.C. Byram, J.J. Dahl, Short-lag spatial coherence of backscattered echoes: imaging characteristics, IEEE Trans. Ultrason. Ferroelectr. Freq. Control 58 (2011) 1377–1388.

[20] J.A. Jensen, Field: A program for simulating ultrasound systems, Med. Biol. Eng. Comput. 34 (1996) 351–353.

[21] J.A. Jensen, N.B. Svendsen, Calculation of pressure fields from arbitrarily shaped, apodized, and excited ultrasound transducers, IEEE Trans. Ultrason., Ferroelec., Freq. Contr. 39 (1992) 262–267.

[22] G. Matrone, A. Ramalli, P. Tortoli, G. Magenes, Experimental evaluation of ultrasound higher-order harmonic imaging with Filtered-Delay Multiply And Sum (F-DMAS) non-linear beamforming, Ultrasonics 86 (2018) 59–68.

[23] M. Polichetti, F. Varray, J.C. Béra, C. Cachard, B. Nicolas, A nonlinear beamforming based on *p*–th root compression – application to plane wave ultrasound imaging, Appl. Sci. 8 (2018) 599–613.

[24] C. Frazier, W.O. Jr, Synthetic aperture techniques with a virtual source element, IEEE Trans. Ultrason. Ferroelectr. Freq. Control 45 (1998) 196–207.

[25] M. Bae, M. Jeong, A study of synthetic-aperture imaging with virtual source elements in B-mode ultrasound imaging systems, IEEE Trans. Ultrason. Ferroelectr. Freq. Control 47 (2000) 1510–1519.

[26] J. Kortbek, J. Jensen, K. Gammelmark, Synthetic aperture sequential beamforming, Proc. IEEE Ultrason. Symp. (2008) 966–969.

[27] M. Tanter, J. Bercoff, L. Sandrin, M. Fink, Ultrafast compound imaging for 2-D motion vector estimation: Application to transient elastography, IEEE Trans. Ultrason. Ferroelectr. Freq. Control 49 (2002) 1363–1374.

[28] N. Bottenus, B. Byram, J. Dahl, G. Trahey, Synthetic aperture focusing for short-lag spatial coherence imaging, IEEE Trans. Ultrason. Ferroelectr. Freq. Control 60 (2013) 1816–1826.

[29] G. Matrone, A.S. Savoia, G. Caliano, G. Magenes, Depth-of-field enhancement in Filtered-Delay Multiply and Sum beamformed images using synthetic aperture focusing, Ultrasonics 75 (2017) 216–225.

[30] G. Matrone, A.S. Savoia, G. Caliano, G. Magenes, Ultrasound plane-wave imaging with delay multiply and sum beamforming and coherent compounding, Proc. IEEE Conf. Eng. Med. Biol. Soc. (2016) 3223–3226.

[31] F. Prieur, O.M.H. Rindal, A. Austeng, Signal coherence and image amplitude with the filtered delay multiply and sum beamformer, IEEE Trans. Ultrason. Ferroelectr. Freq. Control 65 (2018) 1133–1140.